

# Computational Fluid Dynamics Modelling of Multiphase Systems in Anaerobic Baffled Reactors

Adebola Bello Ikeoluwa

March 9, 2020

Anaerobic digesters are multiphase systems in which the conversion of organic matter is facilitated by active biomass. The conversion of organic matter involves four reactions: hydrolysis, acidogenesis, acetogenesis, and methanogenesis. Reaction progress and interaction of each anaerobic reaction stage are dependent on reactor design and operation. The characterization of a reactor for the process would require information about reaction kinetics, interphase interactions, and unique phase characteristics, all of which are pertinent factors influencing reactor optimization. Computational fluid dynamics (CFD) models provide insight into the steady-state hydrodynamic behavior of multiphase systems such as Anaerobic Baffled Reactors (ABRs) at multiple operating conditions with minimal empirical tuning. This may be coupled with experimental descriptions of the effects of modeled initial conditions on bio-decomposition kinetics; therefore, fully characterizing the reactor system within certain CFD modeling assumptions.

The manner of phase interactions depends on reactor operation and design. Plug flow reactor operation might involve active biomass dispersions carried in the fluid flow; fluidized bed arrangements will involve different interphase interactions and might require unique CFD modeling techniques and assumptions. The multiphase system in an ABR during regular operation consists of solid particles or biomass, gaseous products of anaerobic bio-decomposition, and a supply of organic material in a liquid medium. ABRs are advantageous because they facilitate staged anaerobic bio-decomposition reactions via active biomass compartmentalization. In this reactor, cultures of active biomass, dedicated to any of the four reactions, can operate under optimal conditions; that is, in the absence of inhibitions from parallel reactions [1].

## 1. Introduction

There are two standard computational modeling techniques for dispersed multiphase systems: The Euler-Euler and Euler-Lagrange method. These differ in computational domain assumptions, computational demand requirements, and the feasibility of complex phenomena depiction [2]. The purpose of the following literature review is the assessment of typical applications of either approach in literature; this includes a review of proposed justifications for the implementation of either technique.

The Euler-Euler approach to multiphase system modeling characterizes the dispersed phase as a pseudo-continuous fluid; lumped parameters such as drag and mass transfer coefficients describe interphase interactions. Da Rosa et al. [3] utilized an Eulerian-Eulerian approach in the two-phase prediction of bubble flow dispersed in a liquid. The simulated systems were two vertically oriented baffled cylindrical bubble columns with a total capacity of 0.125 and 1 m<sup>3</sup>, corresponding to a small and large column of diameter 0.302 m and 0.604 m, respectively. Da Rosa et al. [3] modeled the physical properties of the dispersed gaseous phase in a bubble column as biogas; the study involved the modeling of the gas-liquid interactions as drag forces acting on rigid spheres, 0.001 m in diameter. The drag force was estimated with the Schiller and Naumann correlation.

Da Rosa et al. [3] modeled the liquid phase in a bubble column as an incompressible Newtonian fluid with physical properties of a vinasse and glycerin mixture; a k-epsilon turbulence model was used to determine the liquid-phase turbulence characteristics; The gas phase was assumed to be laminar. The gas-phase physical properties were modeled as biogas. In this case, both the carrier and dispersed phases were modeled as continuous fluids with unique material properties. Euler-Euler model applications in liquid-gas systems, such as airlift reactors, may require finer meshes bounding the dispersed gas phase. This minimizes the possibility of error in gas phase calculations. This resolution improvement incurs a significant fraction of the computational demand associated with Euler-Euler modeling. Dehbi et al. [4] found that the application of the Euler-Euler method in the simulation of a spouted bed required lower computational requirements compared to the Euler-Lagrange approach; the requirements scaled with mesh size and not particle diameter. Da Rosa et al. [3] conducted mesh dependence tests that showed the expected relationship between bubble column mesh fineness and the computational time. Another consequence of the continuous

fluid assumption for the dispersion is the increased difficulty of modeling intra-phase phenomena. In a liquid-gas dispersion, this includes bubble coalescence, breakage, bubble-bubble collisions, and liquid-bubble collisions. Since the bubbled dispersion in each cell is assumed to be uniformly distributed within each computational cell, the intra-phase interactions must be modeled using only macroscopic variables (e.g., turbulent energy dissipation) instead of local variables (e.g., bubble location). This is one of the main disadvantages of the Euler-Euler approach.

The Euler-Lagrange method depicts the continuous fluid phase as a continuum, and the dispersed phase is tracked in a Lagrangian frame of reference. This accounts for complex dispersed-phase interaction phenomena, such as bubble-bubble interactions in gas-liquid dispersion, which are neglected in the Euler-Euler method [2]. This is achieved with discrete modeling of the dispersed phase as opposed to continuous. Dehbi et al. [5] found that the Lagrangian particle tracking approach is applicable for a dilute dispersed phase; in this case, the continuous flow field is not affected, and one-way coupling is applicable. In a continuous flow field, Adamczyk et al. [6] used the four-way coupling technique to describe dispersed- and continuous-phase interactions for higher concentration dispersed phases, such as those encountered in circulating bed reactors (CBRs). Four-way coupling requires interphase interaction terms to be included in the Navier-Stokes equation as well as to the particles to account for the interaction between particles and with the fluid. The dense discrete phase model solver resolves a force balance on particles called parcels; all particles in parcels are related by mass, velocity, and position. Euler-Lagrange models depict higher resolutions of intra-phase interactions in the dispersed phase without compromising interphase interaction calculations; as a result, significant computational demand is incurred. In liquid-gas systems, the hydrodynamic equations governing bubble motion, mass transfer, coalescence, and breakage are considered in addition to the Navier-Stokes equations for the continuous fluid. The computational requirements scale with the number of discrete components of the dispersed phase; particles in liquid-solid dispersions, and bubbles in liquid-gas systems. Adamczyk et al. [6] simulated a simple and complex version of a circulating bed reactor. In this case, the fineness of the mesh was limited by the size of the tracked particles. This is in agreement with findings by Molinere et al. [4] in the simulation of a spouted bed with the Euler-Lagrange method. The system could be fully defined through calculations of relevant parameters and with minimal assumptions. However, the number of control volumes in a fixed volume was limited by parcel dimensions.

Adamczyk et al. [6] and Almohammed et al. [7] contrasted the results of the Euler-Lagrange and Euler-Euler approach of modelling CFB; the simulation results were compared to experimental data from a runs with a pilot scale CFB. Almohammed et al. [7] found that Euler-Euler and Euler-Lagrange methods predicted comparable results. The pressure drop in the CFB riser evaluated using both numerical methods exhibited similar tendencies as the experimental data. However, there were more considerable discrepancies associated with the Euler-Euler method compared to Euler-Lagrange in pressure drop predictions in the CFB. Adamczyk et al. [6] found that the Euler-Euler and Euler-Lagrange approached similar bed heights and pressure drops but with significantly varying gas and particle flow fields; the Euler-Euler method consistently overpredicted the velocity magnitude compared to experiments. Moliner et al. [4] found that the computational demand increases from the implementation of the Euler-Lagrange model in comparison to the Euler-Euler models in CFBs; in addition, the Euler-Lagrange approach to spouted bed multiphase simulation more accurately reproduced the experimental spouted bed performance.

The primary purpose of this research project is to develop a CFD model to predict gas and liquid fluid dynamics and solids movement in a lab-scale ABR. This model will provide a basis for the development of compartment models and future optimization and scale-up studies. A description of the mathematical model and numerical methodology of single- and two-phase flow simulation in an ABR is provided in this report. In addition, preliminary results for single-phase flow through an ABR geometry is discussed.

## 2. Anaerobic Baffled Reactor Operation and Geometry

The geometry evaluated in this report is the simplified version of a lab-scale ABR with a total and working volume of 40 L and 27.5 L, shown in Figure 3. The complete geometry in Figures 1 and 2 has equal dimensions to the simplified ABR in Figure 3. The only difference is the absence of the 45-degree angled baffles and recirculation tubes in the simplified schematic. The reactors consist of four compartments with a working volume of 6.9 L in each compartment; each compartment is separated by 13 mm thick baffles with 10 mm openings to the next stage. Wastewater is fed continuously to the ABR using a peristaltic pump, from left to right in Figure 2. In the configuration in Figure 1 and 2, the wastewater is forced to pass through the sludge in the reactor with down and up-flow movement [1]. This allows for optimal contact between the wastewater and active biomass. All dimensions in Figure 1 and 2 are reported in millimeters.

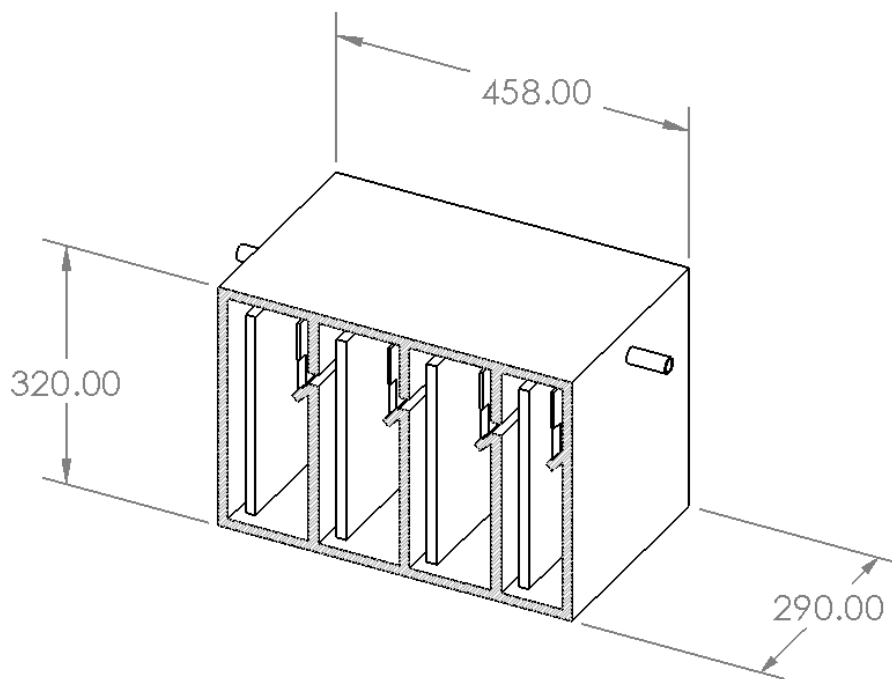


Figure 1. Schematic of the SolidWorks model of the complete anaerobic baffled reactor

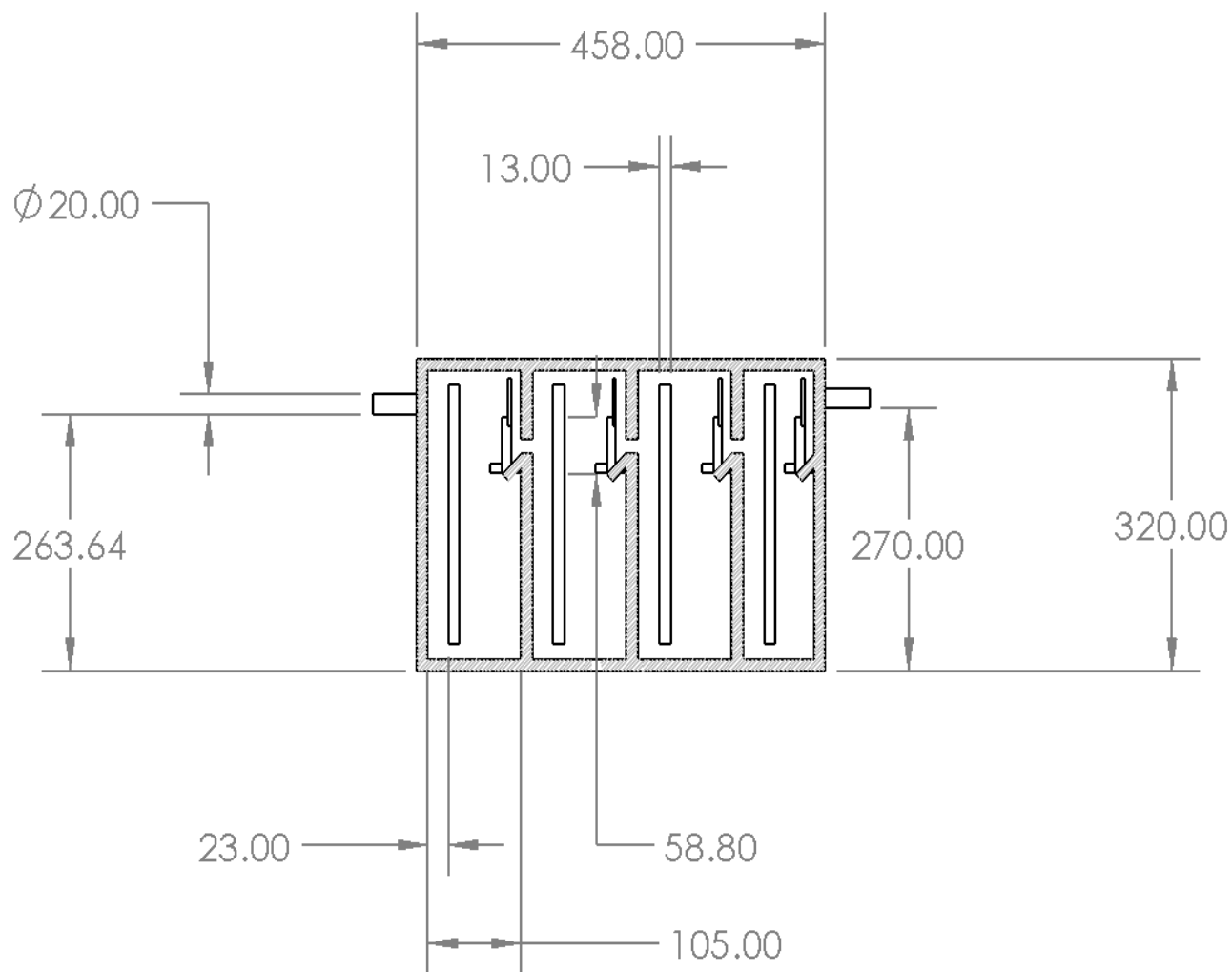


Figure 2. Schematic of the SolidWorks model of the complete anaerobic baffled reactor with additional dimensions

The effluent from the ABR was collected in the buffer tank and then recycled to the inlet by a peristaltic pump to be mixed with the fresh feed. Figure 3 shows the simplified ABR geometry. The simplified and complete geometries have equal dimensions; the only difference is the absence of the 45-degree angled baffles and recirculation tubes in the simplified schematic.

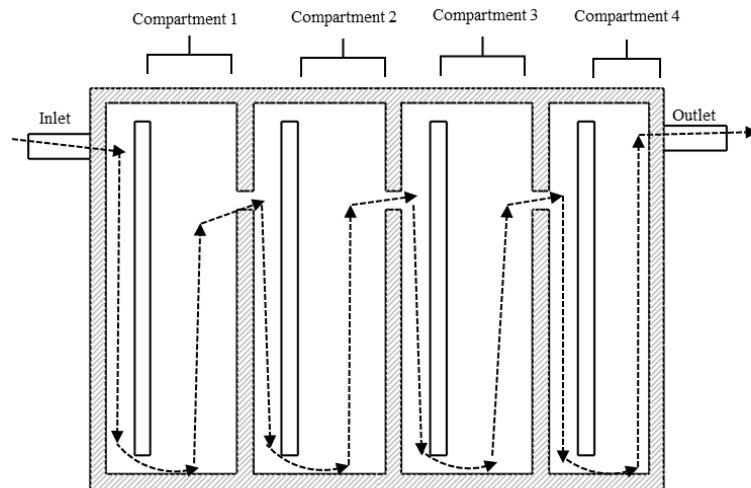


Figure 3. Schematic of the simplified anaerobic baffled reactor which indicates compartment positions and flow patterns in the reactor

### 3. CFD Model Description

The isothermal flow of the liquid and solid phases in a binary multiphase system can be described with a combination of mass and momentum conservation equations. In a control volume, the mass balance for the solid and liquid phase without mass transfer is given by Equation 1 and 2, respectively. In actuality, the phases in an ABR may be characterized as a system of solids and gases dispersed in a liquid phase. In this study, the gaseous phase is assumed to have minimal interactions with the solid and liquid phase in the ABR; therefore, the system may be approximated as a solid dispersion in a liquid phase.

$$\frac{\alpha_s \partial \rho_s}{\partial t} + \alpha_s \nabla \rho_s u_s = 0 \quad (1)$$

where  $\alpha_s = 1 - \alpha_l$

$$\frac{\alpha_l \partial \rho_l}{\partial t} + \alpha_l \nabla \rho_l u_l = 0 \quad (2)$$

A general assumption with both equations is the abundance in the number of particles that constitute each phase, such that discontinuities are negligible. Consequently, the derivatives of various properties exist and are continuous [8]. In Equation 1 and 2,  $\alpha_s$  and  $\alpha_l$  are the phase volume fractions for the solid and liquid phase; for binary systems, the sum of  $\alpha_s$  and  $\alpha_l$  is equal to 1.  $\rho_s$  and  $\rho_l$  are the bulk solid and liquid densities respectively. The ABR system is has three phases, however, the gaseous phase is assumed to not exchange momentum with the solid and liquid phase, and occupies a volume (head space of ABR) with no interaction with rest of the system. The average bulk density of biomass used in experiments with ABR geometry is 1200 kg/m<sup>3</sup> [9]; The average wastewater density may be assumed to be approximately 998 kg/m<sup>3</sup>.

The simplified momentum balance of the respective solid and liquid phases can be described by Equation 3 and 4. The rate of change of momentum of each aliquot moving with a velocity,  $u$ , must be equal to the sum of forces acting each on the phase.



$$\frac{(1 - \alpha_l) \partial \rho_s u_s}{\partial t} + \alpha_s \nabla \rho_s u_s u_s = \sum F_s \quad (3)$$

$$\frac{\alpha_l \partial \rho_l u_l}{\partial t} + \alpha_l \nabla \rho_l u_l u_l = \sum F_l \quad (4)$$

### 3.1. Solid Phase Closure Correlations

In a simplified case of motionless particles dispersed in a stagnant liquid phase, the forces acting on the dispersed solid phase,  $\sum F_s$ , are the liquid pressure and the particle weight [2]. In normal ABR operation, there is a relative velocity between the liquid phase and the settled solid phase. Therefore, the sum of force terms in Equation 3 must account for interactive forces between the liquid and solid phases such as drag, virtual mass, and lift [2]. Virtual mass will not be considered in this study because the biomass in the ABR is initially settled at the base of the reactor and not externally accelerated. In addition, the virtual mass force is negligible when the densities of the two phases are similar. Generally, the forces considered the closure of Equation 3 are drag, buoyancy, weight, and lift.

$$\sum F_s = g(1 - \alpha_l)(\rho_s - \rho_l) + F_{\text{drag}} + F_{\text{lift}} \quad (5)$$

The first term on the right-hand side of Equation 5 accounts for the weight and buoyancy forces acting on the dispersed solid phase.  $F_{\text{drag}}$  and  $F_{\text{lift}}$  are the drag and lift forces. For a solid-gas dispersion in a fluidized bed, and a gas volume fraction less than 0.8, Bird et al. [10], Kunni et al. [11] and Hassan et al. [12] estimated  $F_{\text{drag}}$  with the Ergun equation:

$$F_{\text{drag}} = \beta_e(u_s - u_g) \quad (6)$$

where

$$\beta_e = 150 \frac{(1 - \alpha_l)^2 \mu_l}{\alpha_l (d_s \phi_s)^2} + 1.75 \frac{\rho_l |u_l - u_s| (1 - \alpha_l)}{d_s \phi_s}, \text{ for } \alpha_l < 0.8$$

In this ABR CFD model, the equivalent parameter to gas volume fraction in a gas fluidized beds is  $\alpha_l$ . The active biomass sediment in the ABR may be assumed to be dispersed in a denser liquid medium as opposed to gas; this assumption can provide an estimate of  $F_{\text{drag}}$ . The particle diameter of an active biomass unit is  $0 < d_s < 4.5$  mm [1]. The average liquid viscosity,  $\mu_l$ , of the wastewater treated is approximately 0.00086 Pa s. However, it is possible for  $\alpha_l$  to exceed 0.8 during normal ABR operation;  $\alpha_s$  is generally expected to be between 0.1 and 0.6. Equation 6 may be used to determine  $F_{\text{drag}}$  for ABR simulation cases with large quantities of active biomass,  $\alpha_s > 0.2$ , with variable sphericity,  $\phi_s$ . It is important to note that there is a positive response in cell growth when the chemical oxygen demand in the wastewater stream is increased [1]. The difference is COD concentration between the inlet and outlet multiplied by a growth rate is equal to new biomass generation [1]. Therefore, the particle size distribution, density, and solid phase volume fraction can vary with supplied COD. Table 1 and Table 2 show the particle size distribution at an organic loading rate of 3.5 kg COD/m<sup>3</sup>/day and 1.5 kg COD/m<sup>3</sup>/day respectively.

Table 1. The Size Distribution of Granules in Each Compartment in a Hybrid ABR at 3.5 kg COD/m<sup>3</sup>/day for maximum granule size of 4.5 mm [1].

Compartment	Mean particle size(mm)	% less than 0.5mm	% 0.5-1mm	% 1-1.5mm	% greater than 1.5mm
1	1.01	22	48	17	13
2	0.74	45	37	11	7
3	0.60	50	40	7	3
4	0.37	80	17	3	0

Table 2. The Size Distribution of Granules in Each Compartment in a Hybrid ABR at 1.5 kg COD/m<sup>3</sup>/day for maximum granule size of 4.5 mm [1].

Compartment	Mean particle size(mm)	% less than 0.5mm	% 0.5-1mm	% 1-1.5mm	% greater than 1.5mm
1	0.67	62	20	10	8
2	0.36	90	6	2	2
3	0.31	90	9	1	0
4	0.32	90	7	3	0

The information from Table 1 and 2 shows that the mean particle diameter is less than 1 mm in all compartments of the ABR, and the value reduces proportional to organic loading rate. The mean particle size also reduces from left to right across the ABR.

Sokolichin et al. [13] and Sokolichin et al [14] estimated  $F_{\text{drag}}$ , in Equation 7, for low concentration bubble dispersions in a liquid medium; the dispersed phase volume fraction was less than 0.2 and was modeled as rigid spheres. This volume fraction assumption is reasonable for the dispersed solid phase in the ABR system. Wen et al. [15], Hassan et al. [12] and Moliner [4] also estimated  $F_{\text{drag}}$  with Equation 7 for low particulate concentration fluidized beds, or gas volume fractions greater than 0.8. In this case, the bubble diameter in a low concentration bubble dispersion in liquid [13] can be considered equivalent to a particle diameter in a low concentration solid-gas dispersion [15] in Equation 7 (i.e., similar drag equations can be used if the bubbles are also assumed to be rigid spheres). The effect of other dispersed particles in a fluid is accounted by a correction for stokes particle free-fall law, given as  $f(\alpha_1)$  [16]:

$$F_{\text{drag}} = \beta_s(u_s - u_l) \cdot f(\alpha_1) \quad (7)$$

where

$$\beta_s = \frac{\frac{3}{4}C_D\alpha_1|u_l - u_s|\rho_l(1 - \alpha_1)}{d_s}, \text{ for } \alpha_1 > 0.8$$

$$f(\alpha_1) = \alpha_1^{-2.65}$$

In Equation 7,  $d_s$  is the diameter of the particles in the dispersed phase, and  $\beta_s$  used to determine  $F_{\text{drag}}$  for  $\alpha_1 > 0.8$ . The drag coefficient in Equation 7,  $C_D$ , is related to the Reynolds in Equation 8 [17] [18] for spherical particles.

$$C_D = \frac{24}{Re_s} (1 + 0.15(Re_s^{0.687})) \text{ for } Re_s < 1000, \quad (8)$$

$$C_D = 0.44; Re_s \geq 1000,$$

$$Re_s = \frac{\alpha_1 \rho_l (u_l - u_s) d_s}{\mu_l},$$

Equation 6 and 7 have similar formats;  $\beta_e$  is used to calculate  $F_{\text{drag}}$  for a concentrated dispersed phase while  $\beta_s$  is used for a dilute dispersed phase. However, the volume fraction boundaries which define diluted and concentrated dispersed phases are vague;  $\alpha_1 > 0.8$  are diluted dispersed phases, and  $\alpha_1 < 0.8$  are concentrated. Moliner et al. [4] summarized  $F_{\text{drag}}$  between the fluid phase and dispersed particles for  $0 < \alpha_1 < 1$ . In this case,  $\beta_{es}$  dynamically utilizes the calculated values  $\beta_e$  and  $\beta_s$  for the calculation of  $F_{\text{drag}}$  in Equation 9. As a result,  $\beta_{es}$  is a function of  $\alpha_1$ .

$$F_{\text{drag}} = \beta_{es}(u_l - u_s) \quad (9)$$

where

$$\beta_{es} = \phi_{ls}\beta_s + (1 - \phi_{ls})\beta_e$$

$$\phi_{ls} = \frac{\arctg[262.5(0.2 + \alpha_1 - 1)]}{\pi} + 0.5$$

If a particle with a rigid surface moves in a non-uniform flow field, the flow field may induce a particle rotation around its axis perpendicular to the main flow direction causing a lift force to act on the particle [2]. Almohammed et al. [7] found that the lift force is negligible compared to the drag force as the solid volume fraction approaches 0.8 in fluidized beds. The lift was not included in the momentum balance by Moliner et al. [4] for Eulerian-Eulerian simulation of an internally circulating fluidized bed, solid volume fractions up to 0.6 were tested in the study. However, the lift force is considered in dilute solid-liquid dispersions. This is because the lift force can account for more than half of overall drag in dilute systems and, could govern the trajectory of particles of the dispersed phase [19]. Koerich et al. [20] estimated  $F_{\text{lift}}$  for solid-liquid fluidized bed with an empirical correlation in Equation 10, and the Legendre-Magnaudet model in Equation 11. The maximum dispersed phase volume fraction in the reactor was 0.05, and a local maximum of 0.75-0.95 in the bed. The extent of the contributions of the lift force to the momentum balance of biomass particles in the ABR two-phase system is unclear. However,  $F_{\text{lift}}$  can be estimated with Equation 10 and 11 for a dispersion system with similar volume fraction and phase properties to the ABR system.

$$F_{lift} = (1 - \alpha_l) C_L (\vec{u}_l - \vec{u}_s) (\nabla \times \vec{u}_s) \quad (10)$$

$$C_L = 2.25 \cdot (2 - \exp(2.92 d_s^{2.21})) \cdot (C_{L,lowRe}^2 + C_{L,highRe}^2)^{0.5} \quad (11)$$

where

$$C_{L,lowRe} = \frac{6}{\pi^2 (Re_s Sr_s)^{0.5}} \left( \frac{2.255}{(1 + 0.2E^{-2})^{1.5}} \right) \text{ and } C_{L,highRe} = \frac{1}{2} \left( \frac{1 + \frac{16}{Re_s}}{1 + \frac{29}{Re_s}} \right)$$

In Equation 11,  $Sr_s$  is the strain rate of the particles in the dispersed phase.

In a stationary fluid the settling velocity of a particle can be determined from a force balance on the particle. If lift force is neglected in the force balance, the settling velocity is given by the following equation.

$$U_{sett} = - \left( \frac{4d_s(\rho_w - \rho_s)}{3\rho_w C_D} \right)^{\frac{1}{2}} \quad (12)$$

The forces considered in the derivation to Equation 12 are the weight, buoyancy, and drag forces.  $C_D$  can be determined for the appropriate Reynolds number range with Equation 8. In Equation 12,  $\rho_s$  and  $d_s$  represent the density and diameter of the biomass particles, increasing both parameters increases the settling velocity. However, Equation 12 does not model the effect of gas bubble adhesion to biomass particles on the settling velocity. If the adhesion force is assumed to be sufficient for all bubble diameters, the effective diameter and density can be calculated for a particle and bubble adhesion. The effect of the adhesion force of buoyancy of particle and bubble diameter combinations is analysed in section 3.6. Equation 12 can be modified by replacing the particle density and diameter with an effective density,  $\rho_{eff}$ , and effective diameter,  $d_{eff}$ . The effective density is an estimation of the density of a particle adhered to a gas bubble; in calculation, the particle is assumed to have hypothetically coalesced with a gas bubble of diameter,  $d_b$ , and density

$\rho_b$ . The effective diameter is the diameter of the coalesced particle and gas.  $d_{\text{eff}}$  and  $\rho_{\text{eff}}$  are given by Equation 13 and 14, respectively.

$$d_{\text{eff}} = (d_s^3 + d_b^3)^{\frac{1}{3}} \quad (13)$$

$$\rho_{\text{eff}} = \left( \frac{\gamma}{1 + \gamma} \right) \rho_b + \left( \frac{1}{1 + \gamma} \right) \rho_s \quad (14)$$

where

$$\gamma = \left( \frac{d_b}{d_s} \right)^3$$

In Equation 14,  $\gamma$  is the fraction of the initial particle volume that is equal to the adhered gas bubble volume. The produced gas is assumed to be methane, with a density of  $0.714 \text{ kg m}^{-3}$ . Therefore settling velocity of a gas bubble adhered to a particle in a fluid is given by Equation 15

$$U_{\text{sett}} = - \left( \frac{4d_{\text{eff}}(\rho_w - \rho_{\text{eff}})}{3\rho_w C_D} \right)^{\frac{1}{2}} \quad (15)$$

### 3.2. Liquid Phase Closure Correlations

The liquid phase experiences an equal and opposite force during interactions with the solid phase [2]. Therefore, the sum of forces influencing the momentum of the liquid phase in Equation 4,  $\sum F_l$ , includes the negative value of the sum of all interactive forces, i.e., drag and lift. In addition,  $\sum F_l$  includes external forces such as gravity and the liquid pressure drop and internal forces such as shear stress. Equation 16 shows all constitutive forces describing  $\sum F_l$ .

$$\sum F_l = -\alpha_l \nabla P_l + \nabla \tau_l - (F_{\text{drag}} + F_{\text{lift}}) \quad (16)$$

In Equation 16,  $\nabla \tau_l$  is the liquid shear stress and can be calculated with mean velocity gradients according to the Boussinesq hypothesis in Equation 17 [8]:

$$\nabla \tau_l = \alpha_l \mu_l [\nabla u_l + (\nabla u_l)^T] \quad (17)$$

### 3.3. Case Study 1

The first case involved the simulation of single-phase laminar liquid flow through the simple ABR geometry; in this case,  $\alpha_l$  is equal to 1, and the interphase interactions and solid mass balance are multiplied by zero. The case was simulated with steady-state and transient solvers in OpenFOAM called `simpleFoam` and `twoPhaseEulerFoam`, respectively. The case was simulated with both solvers to confirm that the velocity and pressure fields shown by the transient solver approach steady-state conditions. The initial velocity was set to 0.0025 m/s in the x-direction for both solvers; this was determined with the standard experimental volumetric flow rate of 72.55 Liters per day [1] and the inlet cross-sectional area of 7.06 cm<sup>2</sup>. A uniform pressure field with a magnitude of zero gauge pressure was applied to the outlet; the velocity field boundary condition was zero gradient. All other faces besides the top face in the geometry were assumed to be walls (no slip condition). The top face was set up as a slip wall with zero shear stress to model the



behavior of an air pocket above the fluid under laminar conditions. Figure 4 and 5 below shows the preliminary results of the simulation with `simpleFoam` and `twoPhaseEulerFoam`.

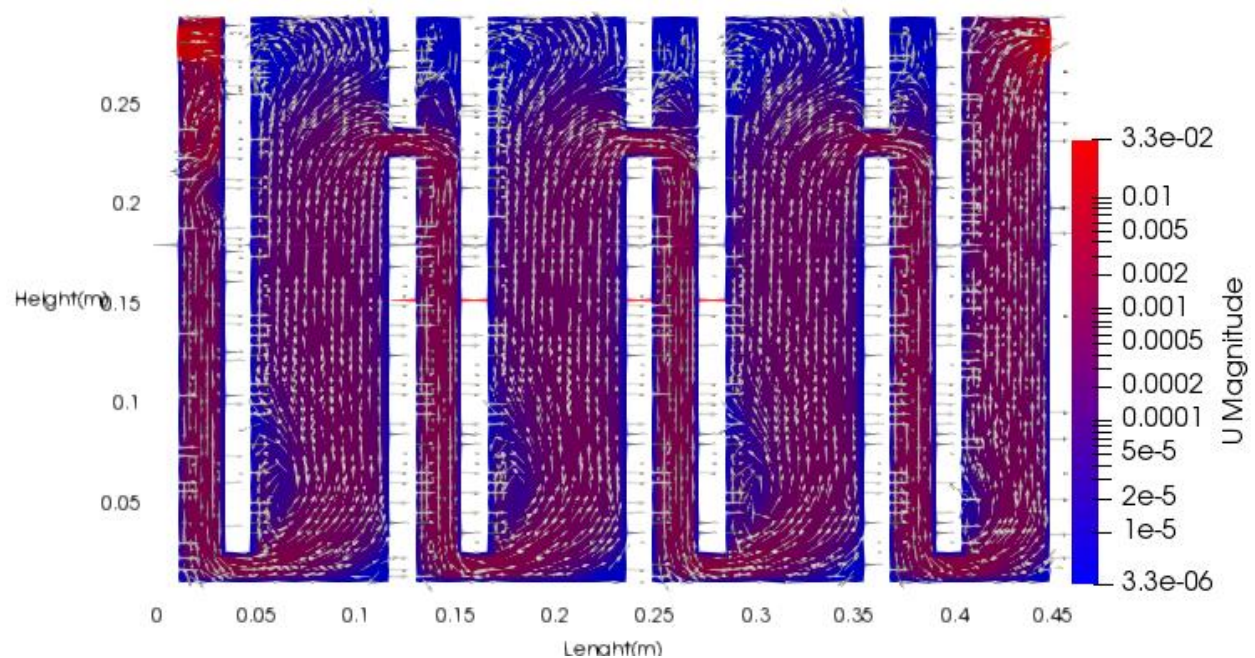


Figure 4. The velocity magnitude graph and fluid flow direction of single-phase flow in simplified ABR geometry simulated with `simpleFoam`

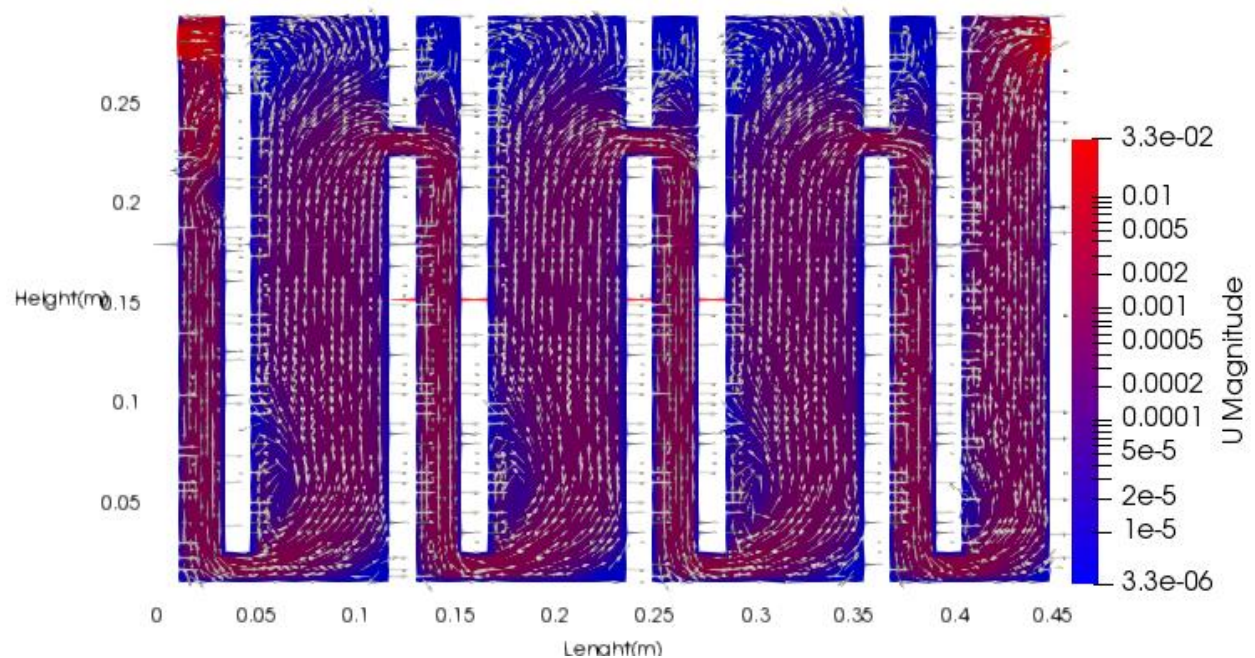


Figure 5. The velocity magnitude graph and fluid flow direction of single-phase flow in simplified ABR geometry simulated with `twoPhaseEulerFoam`

Figures 4 and 5 show the magnitude of the velocity field for fluid flow through the simple ABR geometry. The two solvers show identical final results for the same initial conditions. In both cases, the maximum velocities were observed at the inlet and outlet; there were velocity spikes at flows through the gaps between baffles. This is consistent with the expectation of incompressible flow through the ABR geometry. The velocity spikes at the inter-compartment spaces were a result of the conservation of mass flowrate. In Figure 4, the outlet velocity is higher than the inlet velocity because it has smaller diameter; the outlet and inlet diameters are 15 mm and 20 mm, respectively. The magnitude of velocity is approximately an order less at heights greater than 0.24 m compared to the center of each compartment at the height of 0.12 m. This trend is apparent in the results of both simulations in Figures 4 and 5.

The velocity profiles in each compartment of the ABR are similar. The lowest magnitude of velocity is observed at the walls and baffles. The highest magnitude in a velocity profile drawn on a line parallel to the ABR length typically occurs at the center of each compartment. This is shown in Figure 6.

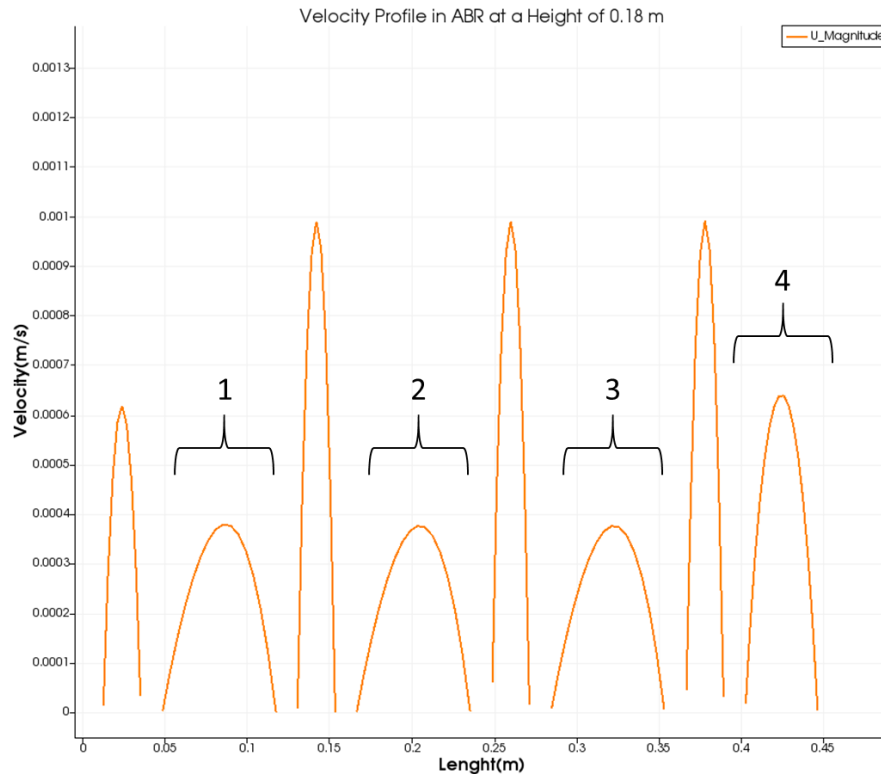


Figure 6. The velocity profile across a line drawn parallel to the length (centered in depth) of the ABR system at the height of 0.18 simulated with `simpleFoam`

In Figure 6, the velocity profile corresponding to the 4<sup>th</sup> compartment has the highest magnitude of all 4 compartments. This is a result of the smaller crosssectional area of the 4<sup>th</sup> compartment. For a constant width, compartment 1 to 3 has a length of 70 mm, while the 4<sup>th</sup> has a length of 50 mm. The velocity profiles between compartments labeled 1 to 4 in Figure 6, corresponds to flow through the small cross-section gap between the baffles leading to each compartment. For a constant width of 290 mm, the annulus has a length of 23 mm. Therefore, flow through the annulus is expected to have a relatively higher velocity compared to each compartment. The velocity profile plot generated with the transient solver at the height of 0.18 m, shown in Figure 7, is identical to Figure 6.

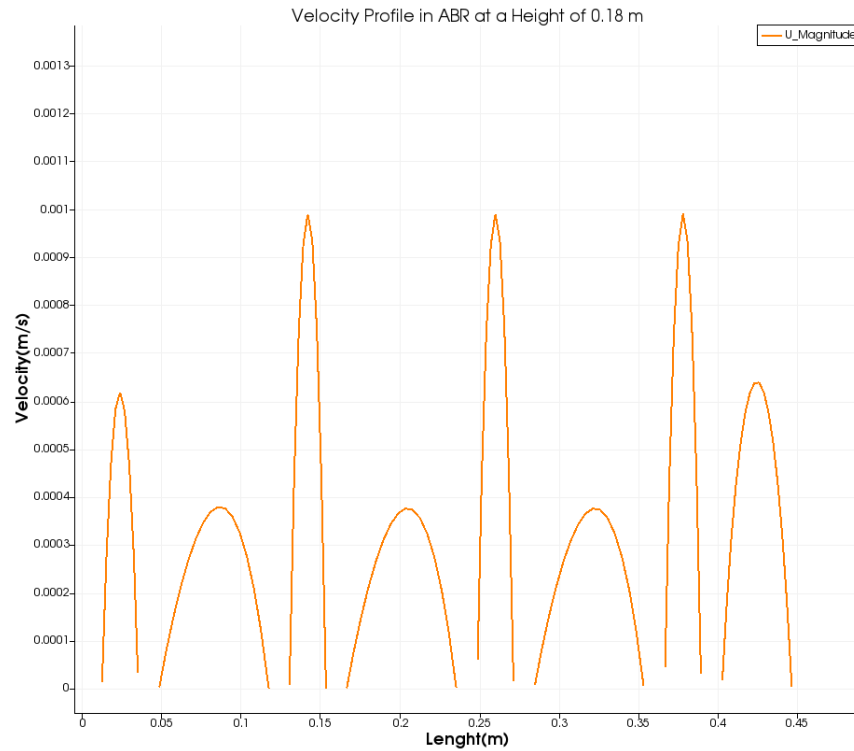


Figure 7. The velocity profile across a line drawn parallel to the length (centered in depth) of the ABR system at the height of 0.18 simulated with `twoPhaseEulerFoam`

### 3.4. Case Study 2

The purpose of this case study is to determine the conditions which favor biomass transfer between compartments. The conditions considered in the study are the settling velocities of the particle in the fluid phase and the magnitude of the fluid velocity in each compartment. An assumption for the case study is that particles with settling velocities greater than the vertical component of the fluid velocity are less probable to carry-over to the next compartment. The effect of particles adhered to bubbles on the settling velocity is also investigated.

The previous case study confirmed that the results of the `twoPhaseEulerFoam` and `simpleFoam` solvers are identical. In addition, the predicted velocity profiles for each compartment are identical. The maximum magnitude of the velocity in each compartment from Figures 4 and 6 is approximately 0.00038 m/s. The velocity in the direction parallel to the ABR

height in each compartment is the dominant contributor to the overall velocity magnitude. This is shown by the velocity profile in the height and length direction for a compartment in the ABR.

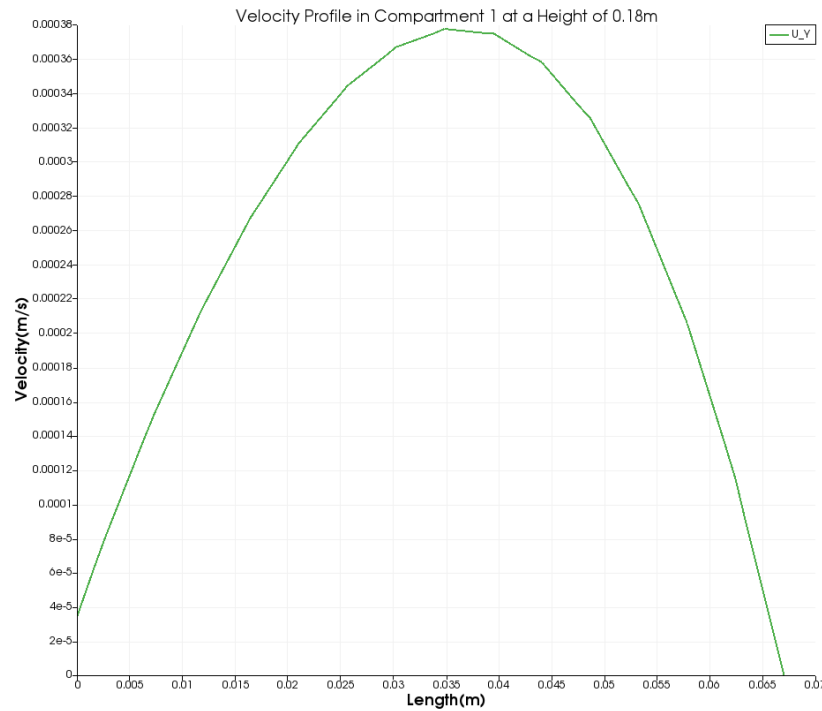


Figure 8. The vertical component velocity profile variation across a line drawn parallel to the length of the 1<sup>st</sup> compartment in the ABR at the height of 0.18.

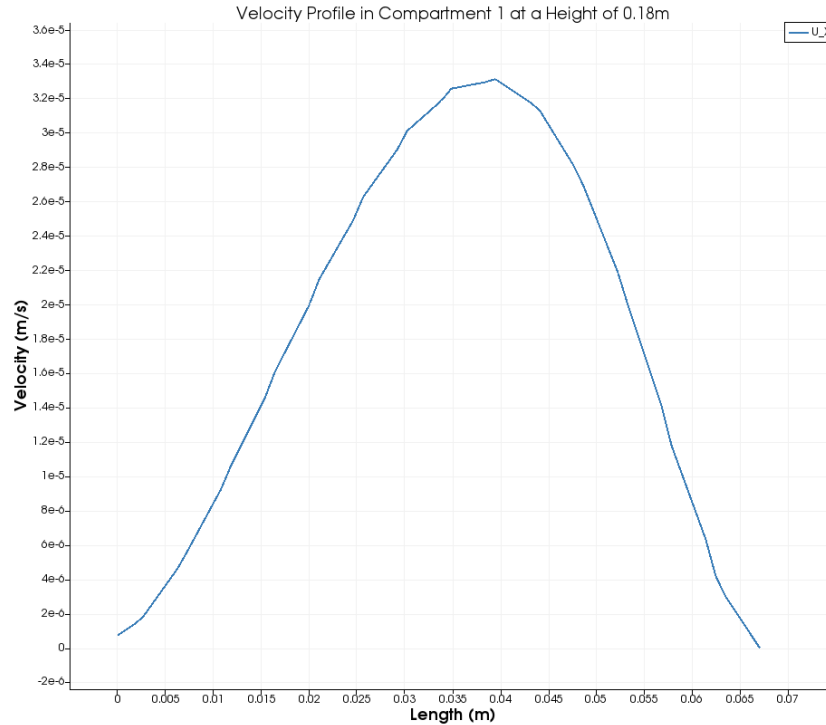


Figure 9. The axial velocity profile variation across a line drawn parallel to the length of the 1<sup>st</sup> compartment in the ABR at the height of 0.18.

From Figure 8 and 9, the maximum value of the velocity in the axial direction  $0.000035 \text{ m/s}$  is an order of magnitude lower than the velocity in the vertical direction. Therefore, the magnitude of the velocity may be assumed to be approximately equal to the magnitude of the y component. This can be shown in Figure 10 to be accurate in the ABR system, with the exception of the velocity magnitude at the inlet, outlet, and the space between baffles. The axial velocity is not zero at a height of 0.18 m because of the proximity to fluid flow through a sudden reduction in crosssectional area. The accelerated fluid between compartments induces a small velocity in close proximity regions; this can be observed in axial velocity profile of the ABR in Figure 10.



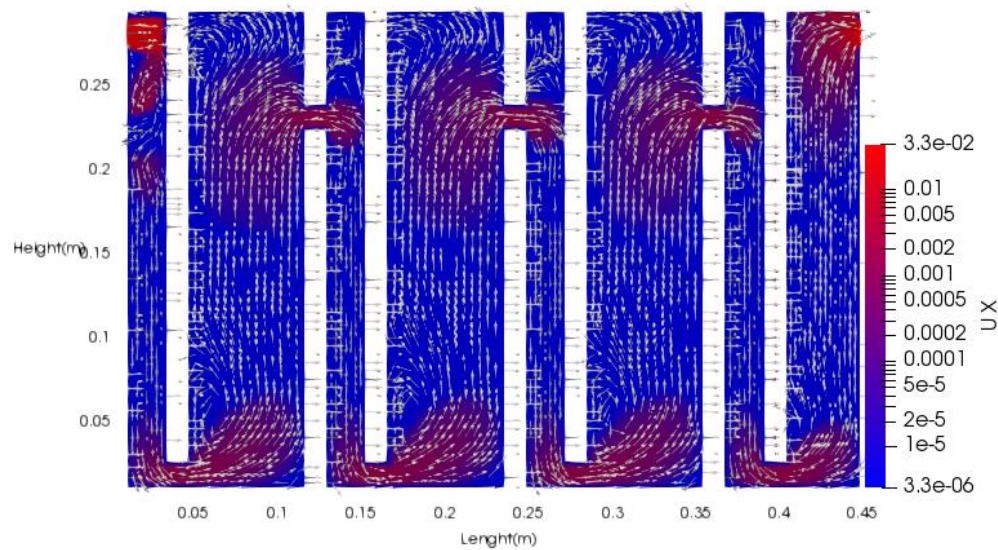


Figure 10. The predicted axial component velocity profile variation in the ABR system.

The effective density of a particle suspended in a fluid reduces as the diameter of the adhered gas bubble increases. Also, the effective diameter of the particle and bubble combination increases as the size of the bubble attached increases. This trend is shown in Figure 11 below.

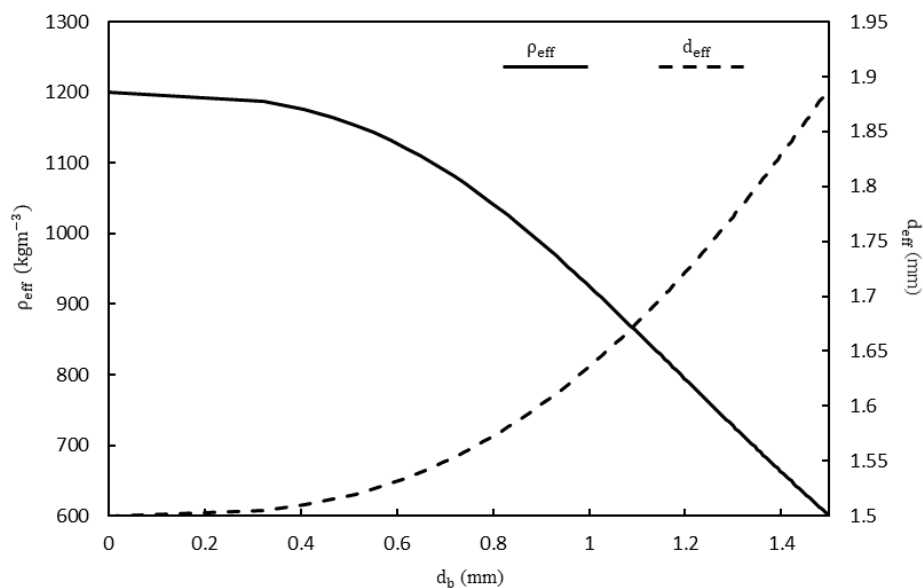


Figure 11. The variation of effective density and effective diameter as a function of the adhered bubble diameter for a 1.5 mm particle

A decrease in the effective density as the effective diameter increases results in a lower weight force acting on the particle. In addition, the increasing effective diameter results in a greater buoyancy force on the particle. The result is a net force in the direction of buoyancy as the effective particle and bubble diameter increases. This trend can be observed in Figure 12 for different particle diameters.

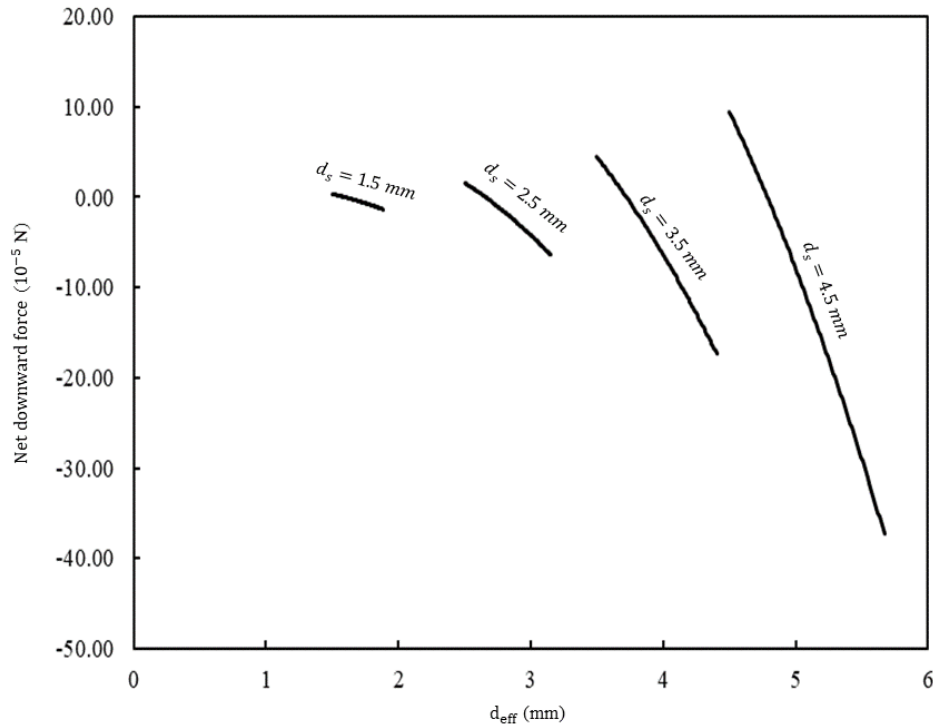


Figure 12. The variation of the net of weight and buoyancy as a function of the effective diameter.

In Figure 12, the dotted line corresponds to the point the adhered bubble diameter is equal to the starting particle diameter. In each instance of the dotted line, the gas volume fraction of the particle and gas bubble mixture is equal to 0.5. For all particle sizes, the buoyant force at a gas volume fraction of 0.5 is greater than the weight of the mixture.

The settling velocity of the particle can be calculated by equating the net of weight and buoyancy to the drag force. The results of the case study of the settling velocity as a function of the adhered bubble diameter for different particle sizes is shown in Figure 13.



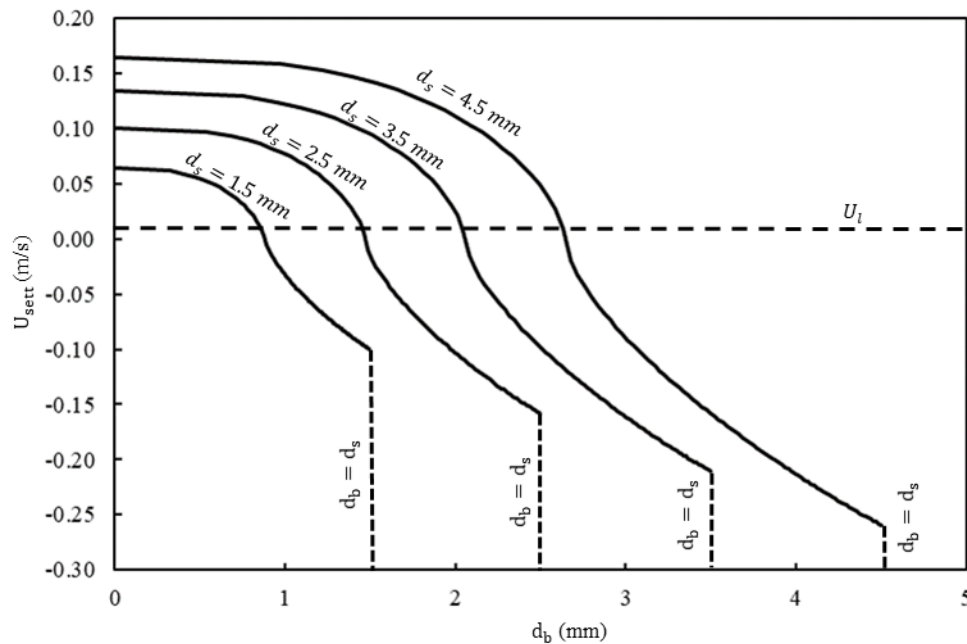


Figure 13. The variation of particle settling velocity with adhered bubble diameter for multiple particle diameters.

The settling velocity of a particle generally decreases as the adhered bubble diameter increases. All particles with bubbles of the same diameter attached have negative settling velocities. In the absence of bubbles, settling velocity for each particle from 1.5 mm to 4.5 mm is greater than the magnitude of fluid velocity in each compartment of the ABR system. However, the settling velocity drops below 0.00038 m/s when a 1.5 mm particle adheres to a 0.89 mm bubble. The same case is predicted in the combination of 2.5 mm, 3.5 mm, and 4.5 mm particles with bubbles with a minimum diameter of 1.49 mm, 2.08 mm, and 2.67 mm, respectively. The minimum bubble diameter and particle size combinations are required for particle carry over to another compartment during ABR operation.

### 3.5. *Bouyant pairs*

In context of this report, a bouyant pair is a combination of a particle and bubble diameters ( $d_s$ ,  $d_p$ ) which results in a negative settling velocity and/or a negative value for the sum of settling velocity, ( $U_{sett}$ ) and liquid velocity ( $U_l$ ). All positive velocities, connote vertically downward

translation in the ABR compartments. Therefore,  $U_l$  in each labeled compartment, in Figure 6, is negative by convention. The flowchart in Figure 14 shows how buoyant pairs are determined.

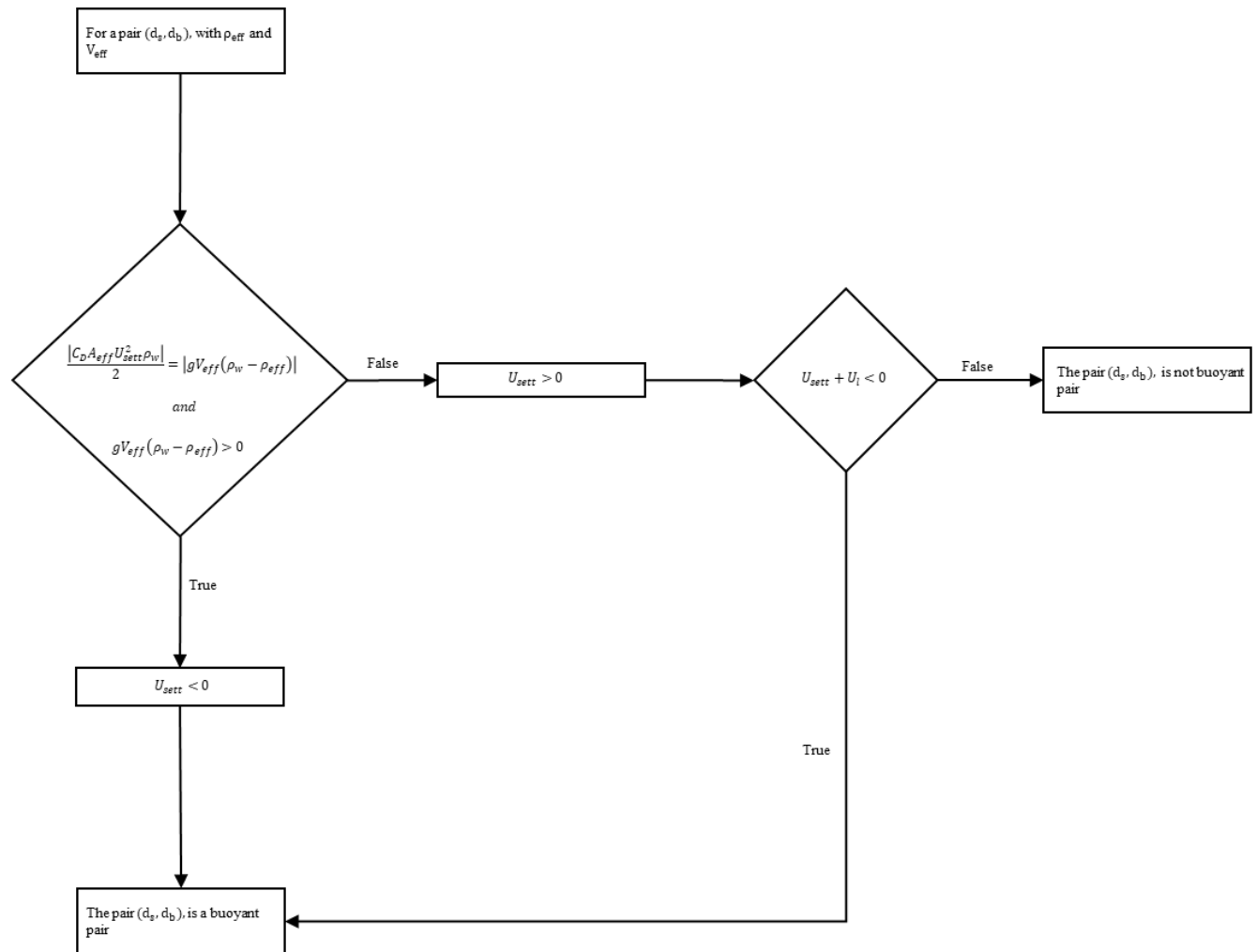


Figure 14. Schematic for the determination of buoyant pairs of particle and bubble diameters.

The schematic in Figure 14 is only applicable, when the settling velocity of the particles alone, is positive and has a greater magnitude than the liquid velocity in the compartment. If this is false, then all combinations of particle and bubble diameters are buoyant pairs. In Figure 13, all values of  $d_b$  mapped to a  $d_s$  curve below the  $U_l$  line are buoyant pairs with the  $d_s$  value represented by the curve, (d<sub>s</sub>, d<sub>b</sub>). From Figure 13, if the liquid velocity increases for a constant particle size distribution, the number of buoyant pairs increases.

### 3.6. Particle-bubble adhesion forces in buoyant pairs

This section is an investigation into the effect of particle bubble adhesion forces on fluid transport of buoyant pairs in the compartments of the ABR. Although the combination is buoyant, particles can only adhere to a gas bubble if the adhesion force is strong enough to compensate the net of the effective buoyancy and weight [21] . As a result, only a fraction of the buoyant pairs can be transported by the fluid. The free body diagram Figure 15 shows the interaction of the forces in the particle adhered to a bubble.

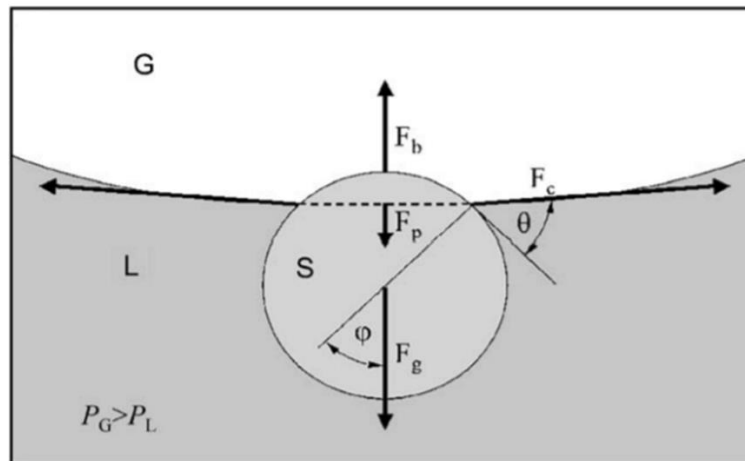


Figure 15. Free body diagram of particle (S), attached to bubble (G) in a liquid phase (L) [21]

In the freebody diagram in Figure 15,  $F_g$  is the effective weight of the the particle and bubble,  $F_p$  is pressure due to capillary pressure inside the gas bubble,  $F_b$  is the effective buoyancy force of the particle and  $F_c$  is the capillary force. The contact angle is given by  $\theta$ , and the penetration angle is  $\phi$ . The adhesion force,  $F_d$  can be defined as the net downward force in Figure 15. The maximum adhesion force,  $F_{d,max}$ , is a function of the three phase contact angle between the particle and bubble [22] [21] [23], the particle diameter and surface tension of the liquid gas interface.

$$F_{d,max} = \pi d_S \gamma_{LG} \sin^2 \frac{\theta}{2} \quad (18)$$

In Equation 18,  $\gamma_{LG}$  is the surface tension water, 0.072N/m. From previous calculations, (1.5, 0.89), (2.5, 1.49), (3.5, 2.08) and (4.5, 2.67) are the buoyant pairs which fall on the  $U_1$  line in Figure 13, and represent the minimum bubble diameters for the buoyant pair criteria. A bubble will be detached from a particle when the net of effective buoyancy and weight (net upward force) exceeds the adhesion force at certain contact angles. The maximum bubble diameter that can attach to a particle is one which causes the net upward force to exceed the maximum adhesion force at all contact angles.

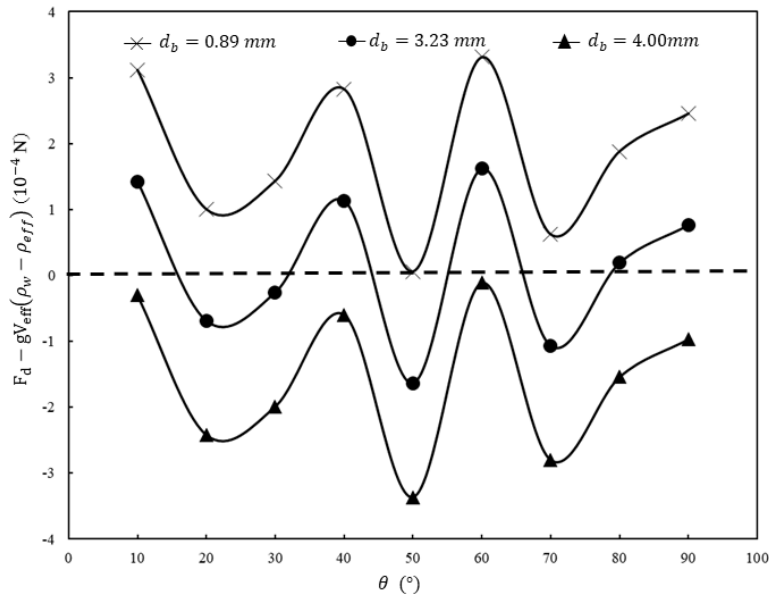


Figure 16. The difference between the adhesion force and the net upward force of various bubble diameters attached to a 1.5mm particle diameter at different contact angles.

In Figure 16, all values below the 0 line represent combinations of bubble diameters and contact angles which result in detachment from a 1.5mm particle. The minimum bubble diameter required for buoyancy, 0.89 mm has adhesion forces greater than the net upward force across all contract angles. Therefore, a 0.89 mm bubble will remain attached to a 1.5mm particle across all contact angles.

The highest adhesion force for all bubble diameters occurs at a contact angle of 60°. As the attached bubble diameter increases, the net upward force increases, and exceeds the adhesion force at

certain contact angles. A 3.23mm bubble would remain attached to a 1.5 mm particle at contact angles of  $10^\circ, 40^\circ, 60^\circ, 80^\circ$  and  $90^\circ$ . The net upward force of a 1.5 mm particle attached to a bubble with a diameter of 4 mm is greater than the adhesion force at all contact angles. Therefore a 1.5 mm particle can be attached to bubbles within the range of  $0.89\text{mm} < d_b < 4.00\text{mm}$ ; bubble diameters higher than 0.89 mm require specific contact angles to maintain adhesion with the particle. A similar trend is observed with a 2.5mm, 3.5mm and 4.5mm particle in Figure 17, Figure 18 and Figure 19, respectively.

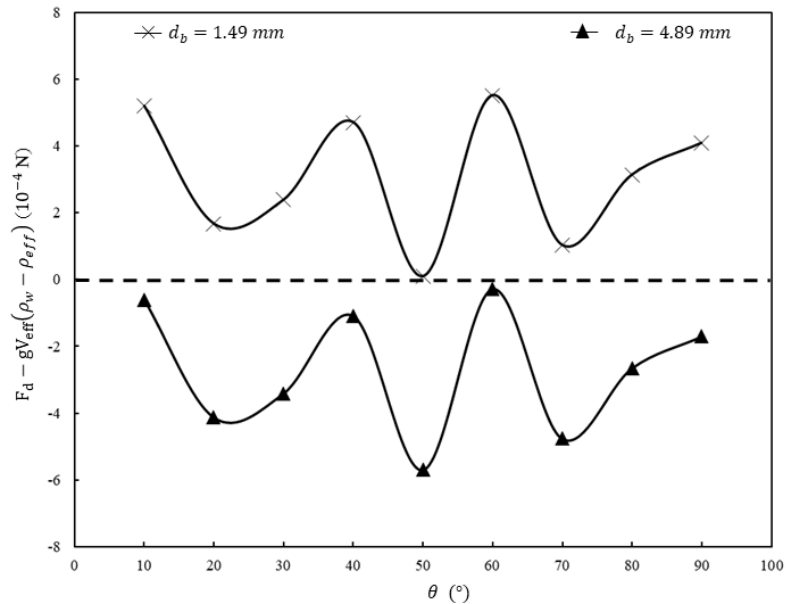


Figure 17. The difference between the adhesion force and the net upward force of various bubble diameters attached to a 2.5mm particle diameter at different contact angles

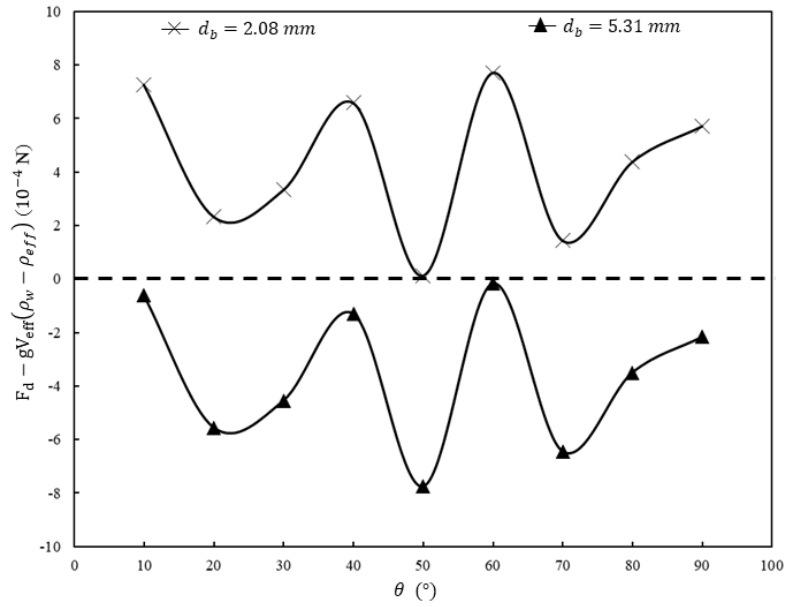


Figure 18. The difference between the adhesion force and the net upward force of various bubble diameters attached to a 3.5 mm particle at different contact angles.

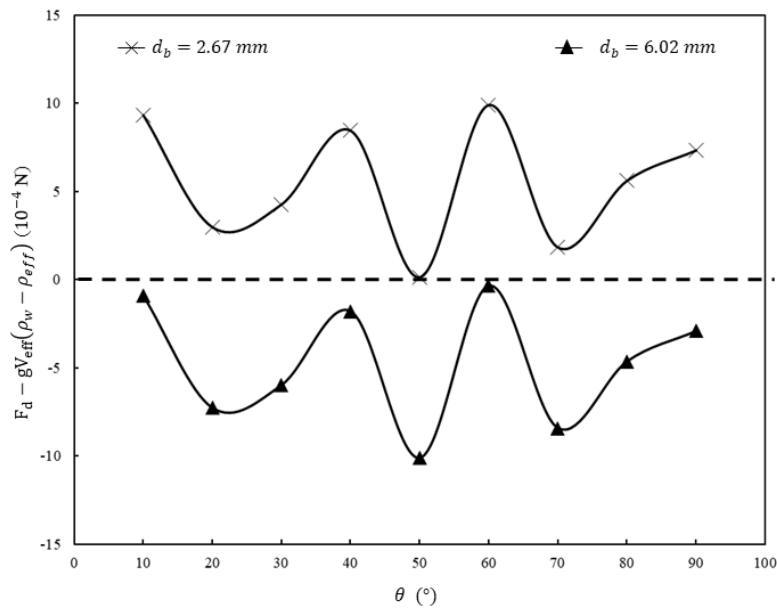


Figure 19. The difference between the adhesion force and the net upward force of various bubble diameters attached to a 4.5 mm particle at different contact angles.

From Figure 17, 18 and 19, a 2.5 mm, 3.5mm and 4.5 mm could be adhered to bubbles with diameters ranging from;  $1.49 \text{ mm} < d_b < 4.89 \text{ mm}$ ,  $2.08 \text{ mm} < d_b < 5.31 \text{ mm}$  , and  $2.67 \text{ mm} < d_b < 6.02 \text{ mm}$ , respectively. The maximum adhesion force increases as the as the particle diameter increases; therefore larger attached bubbles diameters (net upward forces) are feasible.

#### 4. Conclusion and future works

The simulation of the ABR system with transient and steady state solvers with the same initial conditions yield identical pressure and velocity fields. The velocity the profile in each compartment of the ABR system is identical at steady state. The exception to this is velocity profile of the 4<sup>th</sup> compartment; the compartment has the highest maximum velocity of the four compartments because of the relatively smaller crosssection. The height or y component of the velocity in each compartment can be assumed to be equal to the overall magnitude of velocity except in the inlet, outlet and the space between baffles.

The maximum vertical component of the fluid velocity in each compartment is always lower than the settling velocity for the range particle sizes considered in calculation. However, inceasing the diameter of the bubbles attached to partcles significantly reduces the settling velocity. The calculation results showed that a minimum bubble diameter of 1.49 mm, 2.08 mm, and 2.67 mm, is required to reduce the settling velocity of 1.5 mm, 2.5 mm, 3.5 mm, and 4.5 mm particles respectively below the fluid velocity.

The maximum bubble diameter,that can attach to a particle is one which causes the net upward force to exceed the the maximum adhesion force at all contact angles. The maximum bubble diameter than can be attached to a 1.5mm, 2.5mm, 3.5mm and 4.5mm particle are 4.00mm, 4.89 mm, 5.31mm, and 6.02mm respectively. These calculations were done with the assumption of smooth spherical particles in a hydrostatic system. However, the biomass particles in the bed have non-spherical particles of varying aspect ratios and roughness. A study could be completed in the future to analyze the effect of particle roughness and sphericity on the upper limit of the feasible adhered bubble diameters.



## References

- [1] F. Sayedin, "An Integrated Biorefinery for Anaerobic Digestion of Thin Stillage and Microalgae Cultivation for Nutrient Recycling, Bioenergy and Bioproduct Production," Dalhousie University , Halifax, 2019.
- [2] T. Panda, *Bioreactors: Analysis and Design*, Chicago : McGraw-Hill Education Private Limited, 2011.
- [3] L. M. da Rosa, L. Pederivaa, G. Z. . Maurinaa, L. L. Beal, A. P. Torres and M. Sousab, "CFD Analysis of the Effect of Baffle Plates on the Fluid Flow in an Anaerobic Sequencing Batch Reactor," *Chemical Engineering Transactions*, pp. 133-138, 2014.
- [4] C. Moliner, F. Marchelli, N. Spanachi, A. M. Felipe, B. Bosio and E. Arato, "CFD simulation of a spouted bed: Comparison between the Discrete Element Method (DEM) and the Two Fluid Model (TFM)," *Chemical Engineering Journal*, pp. 1-11, 2018.
- [5] A. Dehbi and S. Martin, "CFD simulation of particle deposition on an array of spheres using an Euler/Lagrange approach," *Nuclear Engineering and Design*, p. 3121–3129, 2011.
- [6] W. Adamczyk, B. C. Tomasz, R. A. ecki, G. cel and A. Klimanek, "Comparison of the standard Euler-Euler and hybrid Euler-Lagrange approaches for modeling particle transport in a pilot-scale circulating fluidized," *2013 Chinese Society of Particuology and Institute of Process Engineering, Chinese Academy of Sciences*, pp. 129-137, 2013.
- [7] N. Almohammed , F. Alobaid , . M. Breuer and B. Epple , "A comparative study on the influence of the gas flow rate on the hydrodynamics of a gas–solid spouted fluidized bed using Euler–Euler and Euler–Lagrange/DEM models," *Powder Technology*, p. 343–364, 2014.
- [8] D. Gidaspow, *Multiphase Flow and Fluidization*, San Deigo : Academic Press , 1934.

- [9] B. Connolly, A. Essington, C. Mclean and C. Petersen , "Design of an Anaerobic Baffled Reactor to Remove Organic Content in Thin Stillage Produced from Bioethanol Facilities," Dalhousie University , Halifax, 2015.
- [10] B. R. Bird , W. E. Stewart, N. L. Edwin and D. J. Klingenberg, Transport Phenomena, New York: John Wiley and Sons, 1960.
- [11] D. Kunni and O. Levenspiel, Fluidization Engineering, New York: John Wiley and Sons, 1969.
- [12] M. Hassan , H. Lu, G. Liu, S. Wang and M. Rafique, "Eulerian-Eulerian Simulations of The Hydrodynamics of a Binary Mixture in an Internally Circulating Fluidized Bed," *Brazilian Journal of Chemical Engineering*, pp. 1333-1342, 2018.
- [13] K. Sokolichin and G. Eigenberger, "Gas-liquid Flow in Bubble Columns and Loop Reactors Part1. Detailed Modelling and Numerical Simulation," *Chemical Engineering Science*, pp. 573-5746, 1994.
- [14] A. Sokolichin, G. Eigenberger , A. Lapin and A. Luebert, "Dynamic Numerical Simulation of Gas-Liquid Two Phase Flows Euler/Euler versus Euler/Lagrange," *Chemical Engineering Science*, pp. 611-626, 1997.
- [15] C. Wen and Y. Yu, "Mechanics of Fluidization," *Chem. Eng. Prog. Symp. Series*, p. 100, 1966.
- [16] B. Ettehadieh and D. Gidaspow , "Fluidization in Two-Dimensional Beds with a Jet, Part II," *I&EC Fundamentals*, pp. 193-201, 1983.
- [17] P. Rowe, "Drag Forces in a Hydraulic Model of a Fluidized Bed Part II," *Trans. Inst. Chem. Engs. ,* pp. 175-180, 1961.
- [18] L. Schiller and Z. Nuemann, "A Drag Coefficient Correlation," *Zeitschrift des Vereins Deutscher Ingenieure*, pp. 318-320, 1933.

- [19] I. Mema, V. Mahajan, B. W. Fitzgerald, H. Kuipers and J. T. Padding, "Effect of lift force on dense gas-fluidized beds of non-spherical particles," in *12th International Conference on CFD in Oil and Gas, Metallurgical and Process Industries*, Norway, 2017.
- [20] D. M. Koerich, G. C. Lopes and L. M. Rosa, "Investigation of phases interaction and modifications of drag models for liquid-solid fluidized bed tapered bioreactors," *Power Technology*, vol. 330, pp. 90-101, 2018.
- [21] F. Omata , A. Dimian and A. Blik, "Adhesion of solid particles to gas bubbles, part 1: Modelling," *Chemical Engineering Science*, vol. 61, pp. 823-834, 2006.
- [22] "Direct measurement of bubble-particle adhesion forces on the effects of particle hydrophobicity and surfactants," *IchemE; Chemical Engineering Research and Design* , vol. 82, pp. 490-498, 2004.
- [23] M. L. Fielden, R. A. Hayes and J. Ralston, "Surface and capillary forces affecting air bubble particle interactions in aqueous electrolyte," *Langmuir*, vol. 12, no. 15, pp. 3721-3727, 1996.
- [25] D. Gidaspow, R. Bezburuah and J. Ding , *Hydrodynamics of Circulation Fluidized Beds; Kinetic Theory Approach*, Chicago: Dept. of Chemical Engineering, 1991.